Influence of Thermomechanical Shrinkage on Macrosegregation during Solidification of a Large Size High Strength Steel Ingot

C. Zhang, D. Shahriari, A. Loucif, H. Melkonyan and M. Jahazi

Article published in *International Journal of Advanced Manufacturing Technology*, Volume 99, September 2018, p. 3035-3048

The final publication is available at https://doi.org/10.1007/s00170-018-2695-1

Influence of Thermomechanical Shrinkage on Macrosegregation during Solidification of a Large Size High Strength Steel Ingot

C. Zhang[1] · D. Shahriari[1] · A. Loucif[1] · H. Melkonyan[2] · M. Jahazi[1]

[1]Mechanical engineering department, École de Technologie Supérieure, 1100 Rue Notre-Dame West, Montreal, Quebec H3C1K3, Canada

[2]Finkl-Steel-Sorel, 100 Rue McCarthy, Saint-Joseph-de-Sorel, Quebec, J3R 3M8, Canada

C. Zhang
e-mail: chunping.zhang.1@ens.etsmtl.ca
tel.: 001-5143968800-7868
fax: 001-5143968530

D. Shahriari
e-mail: Davood.Shahriari @etsmtl.ca
tel.: 001-5143968800-7536
fax: 001-5143967536

A. Loucif
e-mail: Abdelhalim.Loucif@etsmtl.ca
tel.: 001-5143968800-7868
fax: 001-5143967536

H. Melkonyan
e-mail: hmelkonyan@finkl.com
tel.: 001-4507464030
fax: 001-4507464092

M. Jahazi
e-mail: Mohammad.Jahazi@etsmtl.ca
tel.: 001-5143968974
fax: 001-5143967536

Abstract
Finite element modeling (FEM) validated by experimental work was used to simulate the influence of thermomechanical shrinkage on macrosegregation of alloying elements in a large size ingot of high strength steel. The full algorithms of the filling and solidification process for thermohydraulic and thermomechanic analyses were developed and implemented in the 3D FEM code Thercast®. Material properties were determined by a combination of experimental works, thermodynamic software Thermo-Calc®, a database and literature source. It was predicted that thermomechanical shrinkage decreased the temperature gradients, advanced the initiation of solidification and reduced the solidification time. The above changes resulted in less severe segregation along the centerline, in the zone next to the ingot surface, in the upper section of the ingot and in the hot-top. Thermomechanic model predictions were proved to agree better with experimental results than the thermohydraulic one. The obtained results were interpreted in the framework of the theories on diffusion and solidification of alloyed systems. These findings contribute to a better understanding of the impact of thermomechanical shrinkage in ingot cooling process. They could also be used in industry to improve the quality of large size ingot production and the productivity of high value added steels or other alloys.

Keywords Large size ingot · Steel · Finite element modeling · Solidification · Thermomechanical shrinkage · Macrosegregation

1 Introduction

Ingot casting is the only method for the production of heavy mono-block forgings of multi-component special steels to meet the increased demands from the power-generation industry. Macrosegregation, as a compositional heterogeneity at the scale of the product, is one of the most significant defects occurring during the solidification process. Often post casting operations such as homogenization are sufficient to remove the

extent and severity of macrosegregation in small size ingots; however, in the case of large size ingots (more than 1.5m diameter), it proves difficult to be removed by subsequent thermo-mechanical treatments, and could pose quality problems [1,2].

Due to the significant cost and difficulties for large scale experimental trials, extensive efforts have been devoted to the development of numerical models for the prediction of macrosegregation in heavy ingots [3]. Im et al. [4] simulated the casting process from the filling stage to solidification using a two-dimensional model, and pointed out the necessity to carry out a coupled filling and solidification analysis because the mixed residual and natural convection flow resulting from the filling stage exert an important effect on solidification. Sang et al. [5] numerically studied the possibility of simulating solidification conditions in a large ingot using a relatively small ingot as reference. Li et al. [6] used a three-phase mixed columnar-equiaxed solidification model to study the formation of columnar and equiaxed zones and segregation patterns in a 2.45 ton steel ingot. Combeau et al. [7,8] developed a 2D multiphase model tackling the natural convection flow together with the motion and growth of equiaxed grains to study the development of macrosegregation in a 3.3-ton and a 65-ton steel ingot, and successfully predicted bottom negative segregation zone. Wu et al. [9] modified an equiaxed solidification model to study the globular and dendritic grain growth, and molded non-uniform solute distribution in the interdendritic melt region as well as the species exchange between the extra- and interdendritic melts by the mechanisms of species diffusion and grain growth. However, in the above analyses, the solid is assumed as a rigid, fixed and stationary phase (i.e. thermomechanical shrinkage is ignored). Such assumptions result in inaccuracies because changes in the composition and mechanical properties of the solidified phase are not taken into consideration [10].

Solidification shrinkage and the deformation of the solid skeleton have been numerically studied on several metallic systems, such as Al-Cu [11,12], Pb-Sn [13], and steel [14,15]. Gao et al. [12] established a theoretical model based on the analysis of the redistribution behaviours of gas and alloying elements for predicting porosity formation and segregation in as-solidified Al-4.5wt.%Cu alloys. The results showed that porosity formation in the mushy zone slightly relieved the solute enrichment in the interdendritic liquid, and consequently reduced the solute segregation. Lan et al. [15] developed a 3D FEM model coupled with natural convection, solute and interfacial heat transfer behavior to predict shrinkage porosity and macrosegregation in a 3.3 ton steel ingot. They found that macrosegregation and shrinkage porosity occurred together in the hot top of the ingot. Other researchers studied the effect of solid deformation on velocity flow [11,13], temperature field [14], and macrosegregation in specified zones [13,14]. However, their influence on the final and global segregation patterns is still unclear. In addition, in most of the above works, important variables, such as solidification contraction ratio [14], casting speed [11,12], feeding length [15], or the flow velocity [13], were considered constant due to the unavailability of material temperature-dependent thermomechanical parameters [14], or appropriate modeling tools [16]. Finally, few simulation results have been compared with experimental observations performed under controlled conditions [13].

In the present work, the influence of solidification shrinkage and solid deformation was studied using 3D finite element simulations of mold-filling and solidification in a 40MT (metric ton) ingot of a high-strength steel. Specifically, a thermohydraulic model (TH) was first developed to study heat and solute transport coupled with flow driven by thermosolutal convection (buoyancy-driven flow). Then a thermomechanic model (TM) was developed where thermosolutal transport induced by the combined effects of buoyancy- and shrinkage-induced flow was considered. The numerical studies were realized in the finite element code Thercast® using a two-phase (liquid-solid) multiscale solidification model. Material parameters were determined by physical simulations, directly done in laboratory, using thermodynamic software Thermo-Calc®, from literature, or from Thercast® material database. The thermal boundary conditions for each case were set to be close to the actual industrial operational conditions used for casting of large size ingots. The evolution of solid shrinkage, air gap formation, temperature, solid fraction and melt velocity fields throughout the filling and cooling stages were investigated. The prediction capabilities of the two models were validated with chemical, thermal and dimensional experimental measurements.

For a comprehensive analysis of the solidification process, detailed information on grain nucleation, growth, morphology transition, and their interactions with macrosegregation evolution is required. Considering the model complexity, the high computation cost for a 40MT ingot and the unavailability of all nucleation and transition parameters, these phenomena were not included in the present model.

2 Experimental setup, process and model geometry

The studied material is a modified P20 steel with the nominal chemical composition listed in Table 1. The ingot had a cylindrical shape with 250cm in height and 150cm in mean diameter and was cast in a big-end-up cast iron mold. The interior surface of the mold was corrugated, as shown in Figure 1a, to increase the perimeter in relation to the cross-sectional area of the ingot for increasing cooling rate and minimizing possible cracking of the ingot during solidification. The mold was hot-topped above in 70cm in height with insulating refractory tiles lined inside, and a layer of insulating exothermic refractory board was over laid on the melt top, as shown in Figure 1b. To ensure higher ingot surface quality and low turbulence, the molten steel was bottom poured into the mold at 1570°C with a superheat of 75°C. The filling time was 30min. The temperature of the outside of the mold was monitored continuously throughout the casting procedure using 5 Chromel-Alumel thermocouples (TC, type K) located in specified positions, as presented in Figure 1b. Each thermocouple was cemented into holes drilled 2.5cm into the mold from the exterior surface. Temperature measurements from each thermocouple were made every 90 seconds from the start of the steel pouring until the ingot was removed from the mold.

Table 1 Nominal chemical composition of the studied modified P20 steel (wt.%)

C	Si	Mn	S	Cr	Mo	P	Ni	Fe
0.36	0.4	0.85	0.0023	1.82	0.45	0.01	0.16	balance

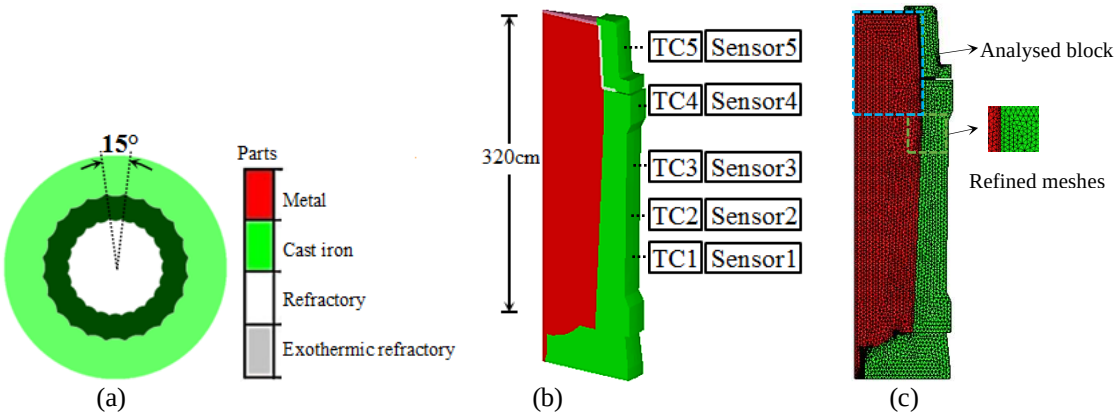

Fig. 1 Casting system and established model. **a** Top view image of the mold. **b** Main elements and corresponding materials in the 15° model with sensors placed in the same positions as the thermocouples (TCs). **c** Mesh distribution of the 15° model

A block comprised of the hot-top and 30cm of the ingot's main body was transversely cut off for the investigation, as the one framed in blue in Figure 1c. Then, two plates ($130\times70\times1.5cm^3$) were sliced on each side of the axial plane, as illustrated in Figure 2. The axial face of one slice (the gray face in the figure) was prepared by grinding and etched in a 50% HCl solution at 50°C to reveal macrosegregation patterns. The other slice was sectioned at regularly-spaced intervals into 250 samples ($6.5\times4.5\times1.5cm^3$). All the faces in the centerline plane along the longitudinal axis (the gray face) were grinded, and then chemically mapped using the Thermo Scientific ARL^{TM} 4460 mass spectrometer.

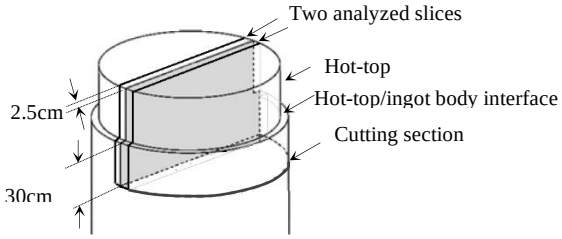

Fig. 2 Cutting diagram for chemical and macrostructure analysis

The chemical composition of each specimen was obtained by averaging out 3 random spectrometer measurements in order to increase accuracy. Then the segregation ratio for each solute element, R^i, was calculated using the relation, $R^i = (\omega^i - \omega_0^i)/\omega_0^i$ [17]. Here, ω^i is the local concentration and ω_0^i is the nominal concentration value. A positive/negative R^i value corresponds to positive/negative segregation. Segregation ratio patterns of different elements in the longitudinal section of the studied block were then reconstructed by interpolation using MATLAB® [18]. This was done by filling the areas between the isolines using constant colors corresponding to the local segregation intensities.

The configuration of the model is displayed in Figure 1b. Due to the symmetry conditions, as shown in Figure 1a, only 15° of the 40MT ingot was modelled. Five sensors were installed at the positions identical to those of the five K type thermocouples. 3D linear tetrahedral elements were used for the spatial discretization of the part and mold components. An average grid of 35mm was selected based on a mesh size optimization analysis. Meshes on the ingot surfaces in contact with molds were refined to approach the true solution, as shown in Figure 1c. Boundary conditions were defined according to the actual industrial practice. For both investigated models, calculations were taken to the moment when the entire casting comes to complete solidification (i.e. around 1400°C).

3 Mathematical formulation

The 3D simulations of mold filling and solidification were performed in the finite element code Thercast®, based on a volume-averaged solid-liquid two-phase model [19]. An Arbitrary Lagrangian-Eulerian (ALE) formulation was used for computing the thermal convection in the liquid pool and mushy zone, and for managing the evolution of metal volume and mass in the mold as a function of time during the filling phase. In contrast, a Lagrangian method was employed for calculating the deformation in solid regions. Sedimentation of equiaxed grains and the deformation of molds were not taken into account in the modeling. In order to simplify the numerical models and reduce the computational cost without altering the accuracy of the results, several assumptions were made:

1) The liquid was assumed incompressible Newtonian and the fluid flow laminar.

2) The mushy region was considered as an isotropic porous solid medium saturated with liquid.

3) Microscopic diffusion of carbon in the solid was assumed to be complete (level rule behavior).

4) Local temperature was considered as a function of the liquid concentration composition ω_l^i and the liquidus slope m_l^i :

$$T = T_m + \sum_{i=1}^{N} m_l^i \omega_l^i \tag{1}$$

where T_m is the melting temperature of the pure iron and N is the number of solute elements in the steel.

5) The heat flux was determined by the law of Fourier and given by the sum of natural convection and radiation contribution:

$$q = -\lambda \nabla T \cdot n = h(T - T_{ext}) + \varepsilon_T \sigma_T \left(T^4 - T_{ext}^4\right) \tag{2}$$

where n denotes the outward normal unit vector, h (W/m/°C) is the heat transfer coefficient and T_{ext} is the external temperature (temperature of the mold), ε_T is the steel emissivity (assumed to be 0.8), σ_T is the Stephan-Boltzmann constant (=5.776×10^{-8}W/m^2/K). The value of heat transfer coefficient h depends on time or on the interface temperature between the part and the mold, simulating the casting/mold contact or loss of contact (formation of air gap) during the cooling of the metal.

6) The solute flux was determined by Fick's law:

$$j = -D_l^i \nabla \omega_l^i \tag{3}$$

where D_l^i is the diffusion coefficient of the chemical element i in the liquid.

7) In the liquid phase, the gravity-driven natural convection loops were created by local density variations [19]. These convective flows are mainly of two types: i) thermal convection flows induced by thermal expansion and temperature gradients, and ii) solutal convection flows induced by solutal expansion and concentration gradients:

$$\rho_l = \rho_0 \left(1 - \beta_T (T - T_{ref}) - \sum_{i=1}^{n} \beta_{\omega^i} (\omega_l^i - \omega_0^i)\right) \tag{4}$$

Here, ρ_l is the density of the liquid, ρ_0 is the reference density taken at the reference temperature T_{ref} (imposed equal to the liquidus temperature), β_T and β_{ω^i} are the thermal and solutal expansion coefficients, respectively, T is the temperature, ω_l^i is the solute concentration in liquid, and ω_0^i is the initial solute concentration mass fraction for solute element *i*.

For the TH model (thermohydraulic model), a constant alloy density was considered during solidification (i.e. $\rho = \rho_l$) so that the solid was assumed to be rigid and stationary. In contrast, for the TM model (thermomechanic model), the density evolved as a function of liquid and solid phases, i.e. $\rho = f_l\rho_l + f_s\rho_s$. Based on the above assumptions, the analysis of fluid flow, temperature, and solute distribution in a solidifying material amounts to the coupled solution of the equations stating the conservation of mass, momentum, energy and solute. For the TM model, a coupled computation of the stress fields is also performed. The detailed derivation of associated auxiliary equations can be found in reference [19] and they will not be repeated here. The variables and their definitions mentioned above and hereinafter are listed in Appendix 1.

4 Determination of material properties

Most of the input parameters used in the modeling of macrosegregation are temperature dependent, reflecting thermodynamic, thermomechanic, and thermodiffusion behaviors. Slight variations in such values have been found to influence, often significantly, model results. Schneider et al. [20] found that two different sets of data for partition coefficients and liquidus temperature led to completely opposite simulation results for the solidification of the same steel. Wu et al. [21] pointed out that the poorly estimated nucleation or thermal parameters resulted in major discrepancy in the prediction of columnar-to-equiaxed transition (CET) region. Therefore, significant care must be taken for the selection of these parameters. In the following, the approaches used in the present investigation are presented.

4.1 Steel thermodynamic properties

The temperature dependence of the density (ρ), solid fraction (f_s) and the specific heat capacity (C_p) were determined by means of the computational thermodynamic software, Thermo-Calc® with TCFE7 Steels/Fe-alloys database [22]. The thermal conductivity (λ) of the steel was assumed to follow Miettinen's model below as a function of temperature and phase fraction [23]:

$$\begin{cases} k = f_\alpha k_\alpha + f_\delta k_\delta + f_\gamma k_\gamma + f_l k_l \\ k_\alpha = (80.91 - 9.9269\times10^{-2}T + 4.613\times10^{-5}T^2)(1 - a_1(\omega_0^C)^{a_2}) \\ k_\delta = (20.14 - 9.313\times10^{-3}T)(1 - a_1(\omega_0^C)^{a_2}) \\ k_\gamma = 21.6 + 8.35\times10^{-3}T \\ k_l = 39 \\ a_1 = 0.425 - 4.385\times10^{-4}T \\ a_2 = 0.209 + 1.09\times10^{-3}T \end{cases} \quad (5)$$

where f_δ, f_γ and f_l are the volume fractions of δ-ferrite, γ-austenite and liquid, respectively, determined using Thermo-Calc®, T is the temperature in ºC, ω_0^C is the nominal weight percent of carbon in the steel.

The applicability of the software Thermo-Calc® and Miettinen's model was verified before applying them to the investigated steel. First, the solid fraction of AISI steel 316, the density of pure iron, the specific heat capacity of AISI steel 1040, and the thermal conductivity coefficient of AISI steel 1020 were calculated using Thermo-Calc®/ Miettinen's model. When the obtained values were found to generally agree with the corresponding experimental behaviors gathered from the literatures ([24] for 316 steel and pure iron, [25] for 1040 and [26] for 1026 steels), the software and the model were used to calculate the thermodynamic properties of the investigated steel. The curves used for verifying the applicability of the above approach, as well as the determined thermodynamic properties of the studied steel as a function of temperature, are plotted in Figure 3.

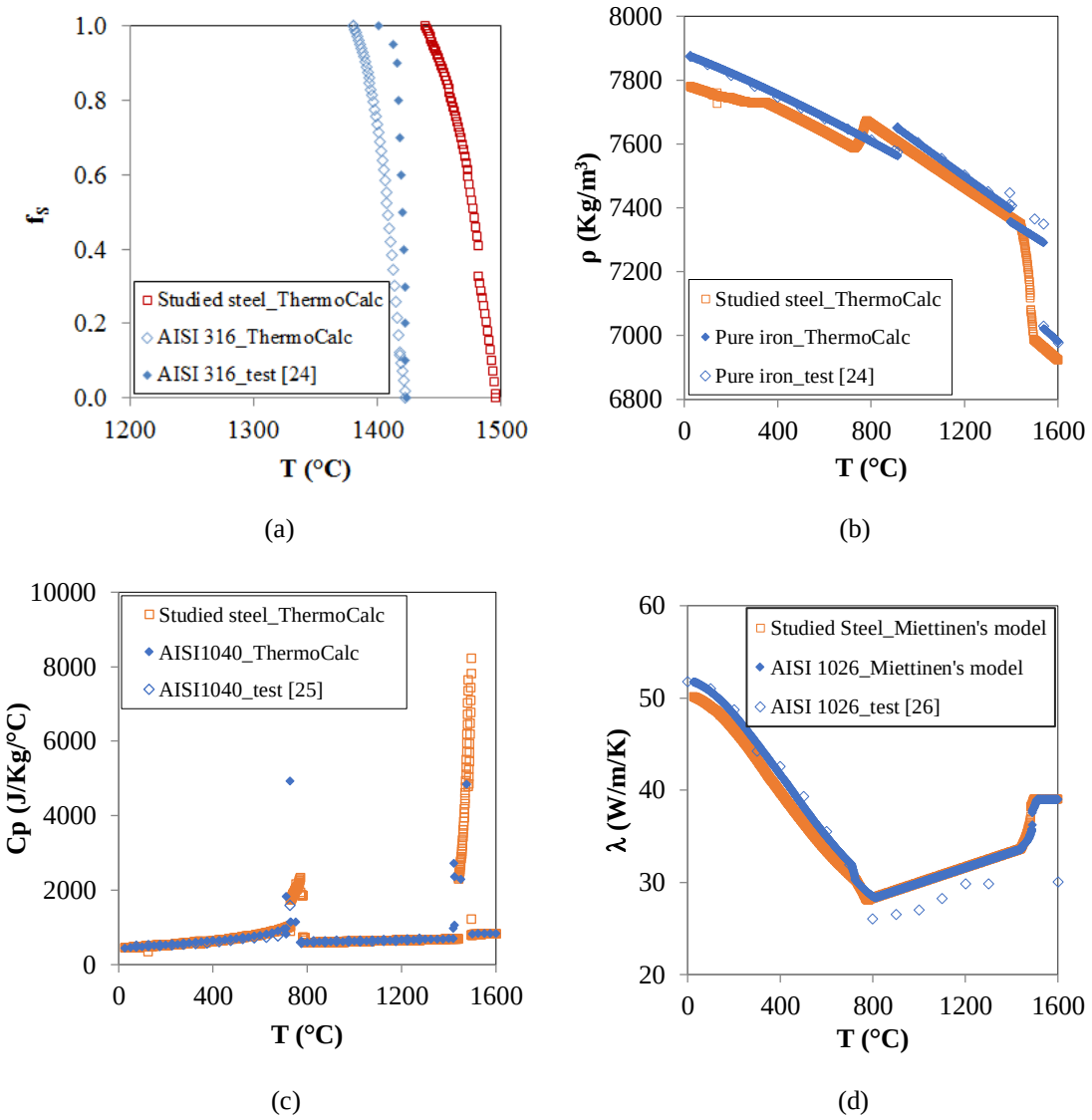

Fig. 3 Temperature dependence of thermodynamic parameters of the studied steel, as well as the calculated and reported properties of pure iron and AISI commercial steels for verifying the applicability of the used software/model. **a** Solid fraction. **b** Density. **c** Specific heat capacity. **d** Thermal conductivity coefficient

4.2 Steel thermomechanical properties

Yield stress (σ_s), Young's modulus (E), strain hardening exponent (n), strain-rate sensitivity coefficient (m) and their variations with temperature were extracted from experimental tensile stress-strain curves, and given in Figure 4. For tensile tests, cylindrical specimens were machined with a diameter of 1cm and a length of 12.2cm with the gauge length of 2.2cm. Tensile tests were performed using Gleeble™ 3800 Thermomechanical Simulator at temperatures of 25, 650, 800, 1000 and 1300°C and strain rates of 10^{-3} and 10^{-4}/s.

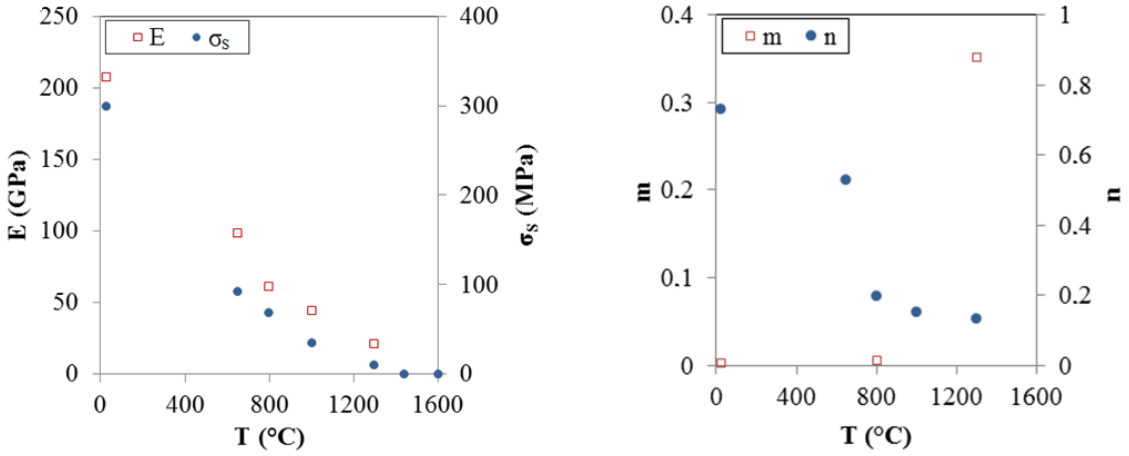

(a) (b)

Fig. 4 Temperature dependence of thermomechanical properties of the studied steel. **a** Young's modulus and yield stress. **b** Stain rate sensitivity and strain hardening coefficient

4.3 Steel thermodiffusion properties

The steel thermodiffusion properties employed in the simulations are presented in Table 2. The equilibrium partition coefficient (k) and the slopes of liquidus line (m_l) were calculated for each element i based on linearized binary phase diagrams with respect to iron, using Thermo-Calc® [22]. The solutal expansion (β_ω) and the diffusion coefficient in the liquid (D) of each element were extracted from references [17,20,27].

Table 2 Thermodiffusion properties for each solutal element

Elements	Symbol	Unit	C	Si	Mn	S	Cr	Mo	P	Ni	Reference
Liquidus slope	m_l^i	K/wt.%	-80.6	-15.7	-5.35	-6.83	-1.66	-2.53	-67.52	-4.82	[22]
Solute partition coefficient	k^i		0.3664	0.7	0.7545	0.0252	0.94	0.837	0.308	0.8474	[22]
Solutal expansion coefficient	β_{ω^i}	$\times 10^{-2}$/wt.%	1.4164	1.19	0.192	1.23	0.397	-0.192	1.15	-0.069	[17,20]
Diffusion coefficient	D^i	mm^2/s	0.02	0.0038	0.0028	0.0042	0.0049	0.0025	0.0016	0.0012	[27]

4.4 Other parameters

The thermophysical properties of all other materials and initial modeling parameters are listed in Table 3. They were obtained from Thermo-Calc® calculations [22], Thercast® material database [19], literature [17,20], experimental measurement, or from the industry. It should be mentioned that the numerical parameters given in Table 3 are for the 15° casting system.

Table 3 Other parameters of the calculation and of the alloys

	Property	Symbol	Unit	Value	Reference
Steel	Reference density	ρ_0	kg/m^3	6.99×10^{-6}	[22]

	Melting temperature of pure iron*	T_m	°C	1538	[22]
	Reference temperature (liquidus)	T_{ref}	°C	1495.3	[22]
	Thermal expansion coefficient	β_T	/K	1.07×10^{-4}	[17]
	Latent heat of fusion	L_f	KJ/Kg	266.8	[20]
	Emissivity	ε_T		0.8	[19]
Cast iron	Density	ρ	kg/m^3	7000	[19]
	Thermal conductivity	λ	W/m/K	30	[19]
Refractory	Density	ρ	kg/m^3	2353	[19]
	Thermal conductivity	λ	W/m/K	1.2	[19]
Exothermic refractory	Density	ρ	kg/m^3	600	-
	Enthalpy of reaction	ΔH	KJ/kg	8373.6	-
	Thermal conductivity	λ	W/m/K	0.2	-
Initial conditions	Steel pouring temperature	T_0	°C	1570	-
	Initial temperature of molds, powders and refractory	T_{mold}	°C	50	-
	Filling time	t	min	30	-
	Exterior environmental temperature	T_{ext}	°C	20	-
Numerical parameters	Number of nodes in the steel part	-	-	10770	-
	Number of elements in the steel part	-	-	46872	-
	Total number of nodes in the casting system	-	-	41192	-
	Total number of elements in the casting system	-	-	182103	-

*Melting temperature of pure iron was used to calculate local temperature as a function of the liquid chemical composition, using Equation (1).

5 Results and discussion

5.1 Top shrinkage and air-gap formation

In contrast to the TH model where no shrinkage and solid contraction are considered, both these phenomena are analyzed in the TM model. To this end, 4 points were selected (as presented on the upper right corner of Figure 5a) to examine the evolution of top shrinkage and lateral air-gap formation as the solidification proceeds. The time dependent vertical displacements of Point 1 (at the top center of the hot-top), and the radial displacements of Points 2 (at the top periphery of hot-top), 3 (at the hot-top/ingot junction skin), and 4

(at the ingot bottom periphery) were monitored. As reported by Point 1 in Figure 5a, the top shrinkage began to appear at the end of the filling stage. Then it developed at a constant rate because of liquid→solid phase change so that after 10h, a vertical displacement of 21cm had taken place. After that, the shrinkage rate slowed down, probably because the contribution of solid deformation caused by the temperature decrease became dominant. Once the bulk metal was completely solidified (15h7min later after pouring), the top shrinkage was close to its final position. The predicted shrinkage depth at the centerline (measured from the original fill height) of about 26cm (≈8% vertical contraction) agreed closely with the cavity dimensions measured on the ingot.

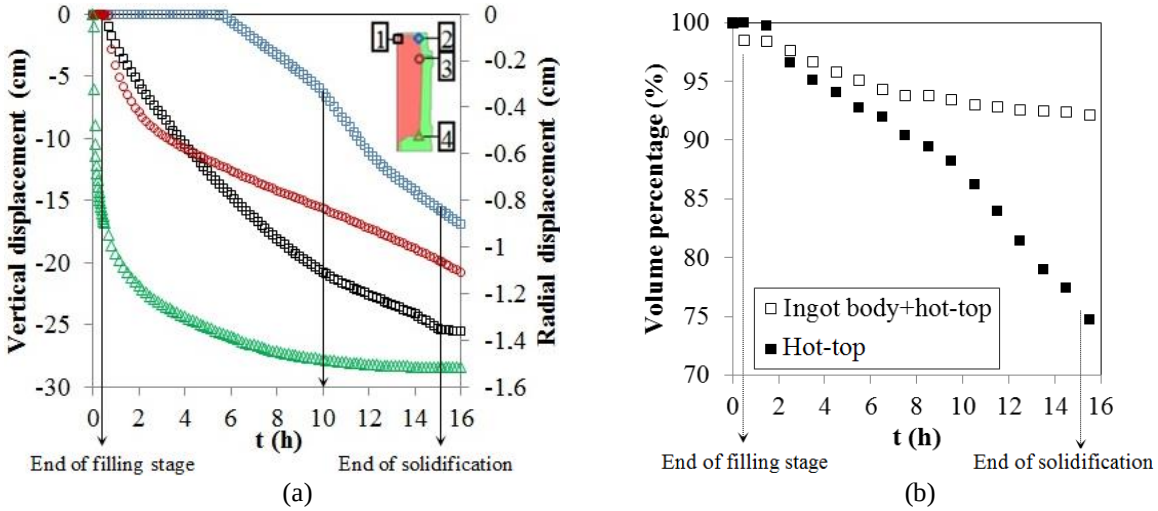

(a) (b)

Fig. 5 Predictions of thermomechanic model (TM). **a** Vertical displacement of Point 1, and radial displacements of Points 2, 3 and 4 with time. **b** Evolution of ingot volume with time

The initiation and development of air gap at different heights of the ingot are also reported in Figure 5a. It can be seen that no radial displacement appeared on Point 2 before 5h and on Point 3 before 0.5h. Such absence of air gap in the hot-top in the early solidification phase could be due to the poor thermal conductivity of the refractory tiles impeding the heat loss in the hot-top. Radial displacements on Point 3 were found to take place at the end of filling, while on Point 4, it occurred at almost the first pouring moment, indicating that the air gap was created below the hot-top/ingot interface section before the end of filling. This early occurrence of air gap could be the result of the ingot solidification shrinkage resulting from the no continuous temperature distribution at the casting/mold interface. The slopes of the radial displacement curves followed by Points 3 and 4 were found to decrease with the time, indicating the gradual decrease in the development rate of the air gap probably owing to the increase of the solid fraction. This different initiation time and growth of the radial shrinkage resulted in a staircase distribution of the air gap size along the ingot skin at the end of solidification: 0.84cm at the top on Point 2 (≈1.2% radial shrinkage), 1.06cm at the hot-top/ingot intersection on Point 3 (≈1.4% radial shrinkage), and 1.5cm at the bottom on Point 4 (≈2.2% radial shrinkage). This predicted air gap values matched well with the radial contraction measurements for the ingot.

The combination of the shrinkage at the top of the ingot and the formation of the radial air gap detached the casting away from the top and the mold walls, leading to a volume reduction, as shown in Figure 5b. The volume reduction of ingot body + hot-top and its variation with time were obtained by measuring the ratio between the instantaneous longitudinal cross-section area of ingot body + hot-top and their initial value before solidification. The shrinkage also resulted in the variation of global shape, as shown in Figure 6, and the change of heat transfer mode from purely conduction to convection and radiation. All the above changes gave rise to different features in the temperature gradient, liquid fraction distribution, fluid flow field, solidification time, and macrosegregation pattern, compared to those predicted with the TH model, as discussed below.

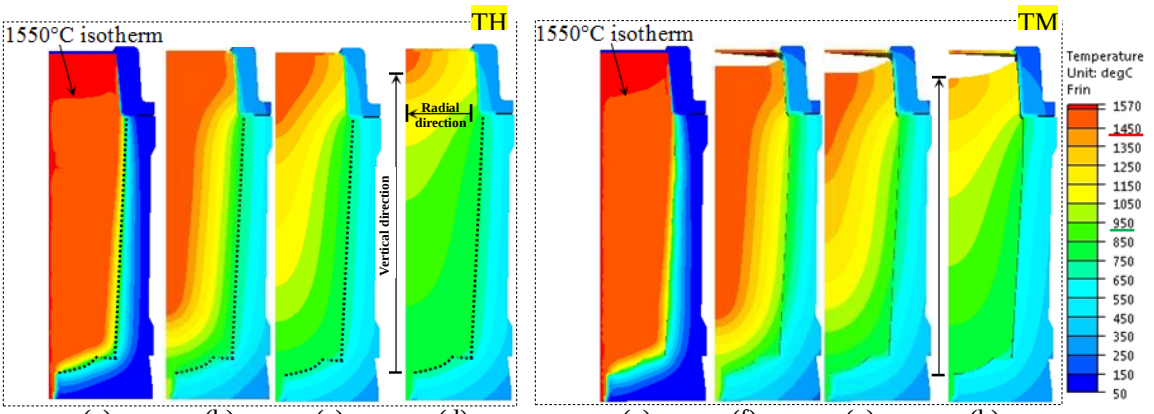

Fig. 6 Temperature fields predicted by thermohydraulic (TH, left) and thermomechanic models (TM, right) at times of: **a e** 0.5h (end of filling). **b f** 5.5h. **c g** 10.5h. **d h** 15.5h after pouring

5.2 Temperature gradient

Temperature gradient patterns at times of 0.5h (end of filling) 5.5h, 10.5h and 15.5h after pouring are shown in Figure 6. The left four figures correspond to the predictions using the TH model and the right four ones are from the TM model. For the TH case, the interface between the ingot and the mold was marked artificially with dashed lines. Two common features can be seen for the thermohydraulic and thermomechanic predictions: (1) at the end of the filling stage, a slight horizontal temperature gradient was developed close to the mold chill wall and a vertical one next to the mold base (Figures 6a and 6e); (2) as solidification proceeded, the horizontal isotherms became inclined and the spacing between the adjacent isotherms widened. The above evolution of temperature isotherms are similar to those reported by Im et al. for pure heat conduction analysis [4].

However, at the end of the filling stage, the TM model presents an inclined isotherm of 1550°C (Figure 6e), in contrast to a horizontal one in the TH model (Figure 6a). This inclination could be attributed to the variation in volumetric contraction that occurs along the ingot skin from the bottom to the hot-top/ingot body interface section. Furthermore, as shown in Figures 6b-6d and 6f-6h, in the late solidification stage (i.e. above 10h after pouring), the vertical and radial temperature gradients predicted by the TM model were smaller than those from the TH model. Above 15h after pouring, as shown in Figures 6d and 6h, the vertical temperature gradient along the ingot axis reached 1.96°C/cm for the TM model and 2.12°C/cm for the TH model; the radial gradient along the hot-top/ingot body interface section was 4.21°C/cm for the TM model and 5.09°C/cm for the TH model.

Examinations of individual isotherms revealed that when considering the mechanical properties of the solid (i.e. TM model), *smaller* thermal gradients were predicted. Figure 7 shows the evolution of isotherms of 1450°C and 950°C with time in the vertical direction along the ingot axis (Figure 7a) and in the radial direction along the hot-top/ingot body interface section (Figure 7b). It can be seen that at any given solidification moment, the distances between the two isotherms predicted by the TM model are larger than those in the TH case.

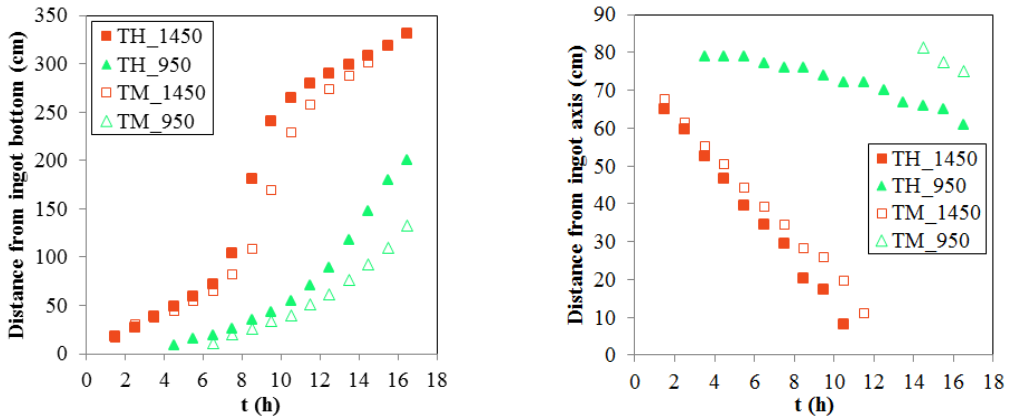

(a) (b)

Fig. 7 Evolution of isotherms 1450°C and 950°C with time. **a** Vertical direction. **b** Radial direction

5.3 Liquid fraction and solidification time

Liquid fraction patterns at times of 0.5h (end of filling) 1.5h, 10.5h and 15.5h after pouring are shown in Figure 8 for both models. It can be seen in Figures 8a and 8e that at the start of solidification, the liquid fraction predicted by the two models is very similar, presenting no distinct action of the mechanical deformation. A metal shell, occupying about 7% of the total mass, formed next to the chill mold wall in the ingot body. Its formation could be associated with the rapid extraction of the initial superheat of the melt from the cold mold, as also reported by Schneider and Beckermann [20].

Furthermore, a comparison of Figures 8c and 8d with 8g and 8h shows that when shrinkage and the mechanical properties of the solid are considered (TM model), solidification proceeds slower before the complete solidification of the ingot body: it takes 10h in the TH model to reach a total solid ingot body, but 11h with the TM model; solidification proceeds quicker and ends earlier after entire solidification of the ingot body.

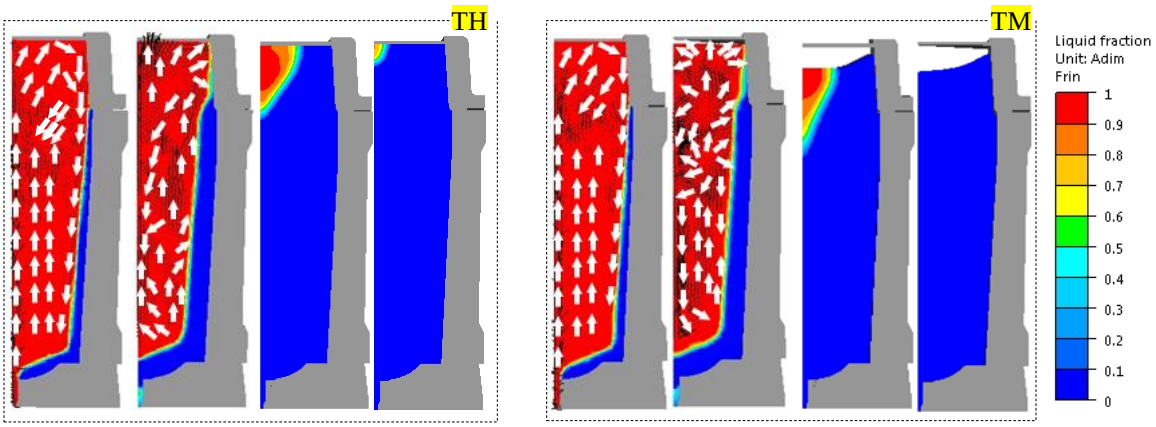

(a) (b) (c) (d) (e) (f) (g) (h)

Fig. 8 Liquid fraction and liquid flow patterns predicted by thermohydraulic (TH, left) and thermomechanic resolution (TM, right) at times of: **a e** 0.5h (end of filling). **b f** 1.5h. **c g** 10.5h. **d h** 15.5h after pouring

Examination of the variation of solid volumetric fraction with time proved the nonuniform solidification rate over the solidification interval. As shown in Figure 9, the solid fraction predicted by the TM model was similar to the one with the TH model for the first 3 hours, but became lower between the 4 and 10 hours (before complete solidification of ingot body), and turned higher after it, until the end of the solidification

process. The lower solid fraction in the second phase could be related to the slower heat-extraction rate due to the formation of the air gap and its insulating effect, as also reported by Chiang and Tsai [11], as well as the downward pulling of the solidification front owing to the formation of the shrinkage cavity at the top. The significant hot-top volumetric contraction in the third phase, as presented in Figure 5b, could be at the origin of the observed higher solidification rate of the ingot in the second phase.

The acceleration in the solidification process caused by thermomechanic deformation was also proved by the solidification time analyses, as shown in Figure 10. For both models, it was predicted that the solidification of the initial superheated melt was initiated almost immediately (8s) after pouring, in the region next to the chill zone, because of the sensible heat loss from the cold mold. The maximum initiation time for the triggering of solidification in the TM model was predicted to be 5h18min. This value is 23min shorter than in the TH model. The total solidification time of 15h7min (54429s, see Figure 10b) obtained with the TM model is 1h47min shorter than when using the purely conduction TH model (16h54min, as shown in Figure 10a). The faster solidification process could be the result of the reduction of ingot body and hot-top volume (as shown in Figure 5b), which could prevail over the insulating function of the air gap in the cooling stage.

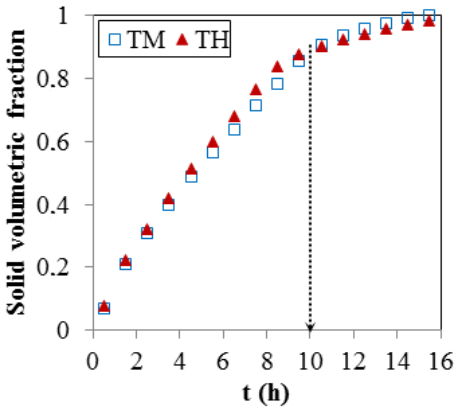

Fig. 9 Evolution of solid volumetric fraction with time

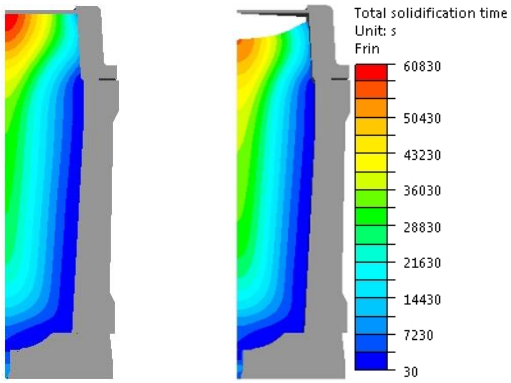

(a) (b)

Fig. 10 Total solidification time patterns. **a** Thermohydraulic model (TH). **b** Thermomechanic model (TM)

5.4 Macrosegregation pattern

As shown in Figure 11, large scale compositional variations were closely associated with the convective flow, and influenced by the above-mentioned changes of temperature gradient and solidification rate. At the start of solidification, the first solid particles formed in the upper part of the ingot body in the TH model (shown by red spots in Figure 11a), while in the TM model, they were formed in the hot-top (shown by red spots in Figure 11e). These different positions could be related to different residual flow modes in the two models, as seen in Figures 8a and 8e. In the TH model (Figure 8a), during mold filling, liquid bulk first moved upward

along the centerline, then flowed downward along the solidification front affected by the local mold configuration. It then diverged toward the less dense core under the influence of lateral thermal gradient, creating clockwise vortex in the upper part where the first solid particles start to form in the melt. In the TM model (Figure 8e), the residual flow driven clockwise vortex was moved upwards due to the radial shrinkage. Therefore, the first particles were formed in the hot-top rather than in the upper part of the ingot. Furthermore, this downward and diverged flow would pass through the low-f_l mushy zone, remelt and consequently channel the mushy zone. This process could be responsible for the formation of positive segregated bands close to the chill zone [28], as observed in Figures 11b-11d and 11f-11h.

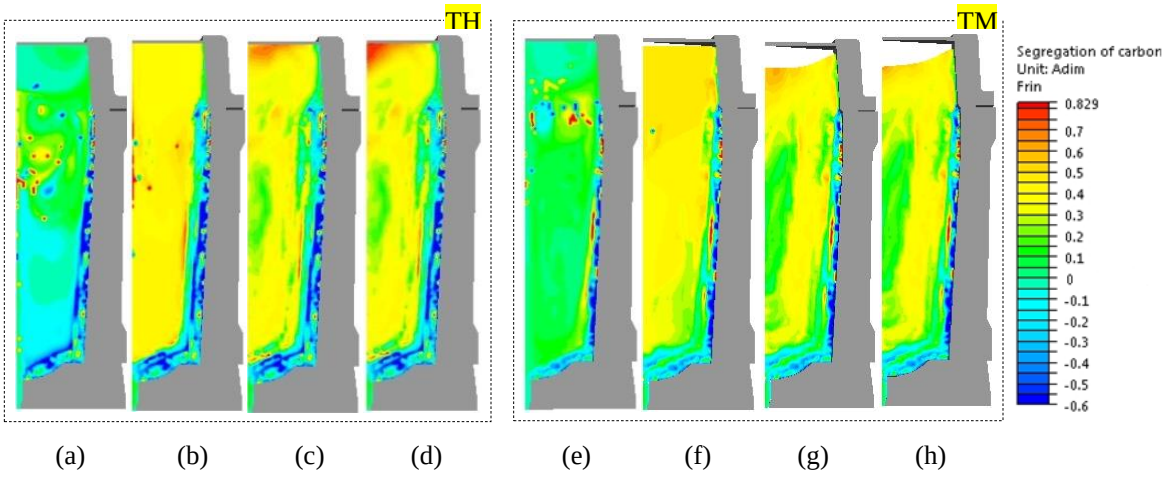

Fig. 11 Carbon segregation ratio patterns predicted with thermohydraulic (TH, left) and thermomechanic models (TM, right) at times of: **a e** 0.5h (end of filling). **b f** 1.5h. **c g** 10.5h. **d h** 15.5h after pouring

During later solidification phase, as compared between Figures 11b and 11f, lower concentrations of solutes along the ingot axis and the solidification front were predicted by the TM model. This finding could be associated with the natural convection flow prevailing in the later stages of solidification under the action of local density variation, as seen in Figures 8b and 8f. In the TH model (Figure 8b), natural convective flow counteracted the downward flow, resulting in the inversion of the initial clockwise movement. In contrast, in the TM model (Figure 8f), mechanical shrinkage disordered this convective flow, and therefore impeded the directed distribution of the rejected solutes and weakened the accumulation trend of solutes along the centerline and in the solidification front. In addition, this lower positive segregation intensity could also originate from the smaller density variations due to the lower temperature gradient resulting from thermomechanic shrinkage.

Ten hours after the filling stage, when the ingot body was almost totally solidified, as illustrated in Figures 11c and 11g, positive segregated zones formed in the center upper region and negative segregated zones at the bottom. Solute-enriched segregation zones were also formed between the center and the ingot wall, as clearly revealed in Figures 11c, 11d, 11g and 11h. They extended nearly over the entire length of the ingot, inclined with respect to the ingot boundaries with a pattern similar to those calculated numerically by Schneider and Beckermann [29]. Finally, it should be noted that as shown in Figure 11d, large spatial variations in composition are predicted with the TH model. Sang et al. [5] also reported similar observations and related it to pure convection-induced flows that are assumed in the thermohydraulic modeling. In contrast, the macrosegregation in the upper section of the ingot and in the hot-top predicted by TM model was comparatively less severe, as seen in Figure 11h. The milder segregation finds its origin in the accelerated solidification in the casting process due to ingot volume contraction as discussed above.

5.5 Validation of models

Temperature profiles on the mold outer surface and the chemical distribution pattern on the longitudinal cross-section of the investigated block were used for the validation of the established models. Predicted temperature variations on the mold's outer surface as a function of time were compared with measured values

of thermocouples (TC) placed at 5 characteristic positions (as illustrated in Figure 1b). As shown in Figure 12, at first, the temperatures sharply increased one after another, reflecting the successive contact between the melt and mold during pouring. Then, the increasing tendency was slowed down because of the heat loss from the mold wall. Temperatures began to decrease about 6 hours after reaching their individual temperature peaks. Owing to the low conductivity of the insulating tiles inside the hot-top mold, the increasing tendency was slowed and the lowest peak temperature value was recorded by TC5. All these features were reproduced by the sensors of the TM model. A very good correlation can be seen between the predicted values by the TM model and the measured values. The 20-50°C difference could be attributed to the uncertainty in the exact values of the thermal conductivity of the cast iron mold and the refractory tiles used in the computations. In contrast, the mold surface temperature evolutions predicted by the TH model predictions did not agree well with TC measurements.

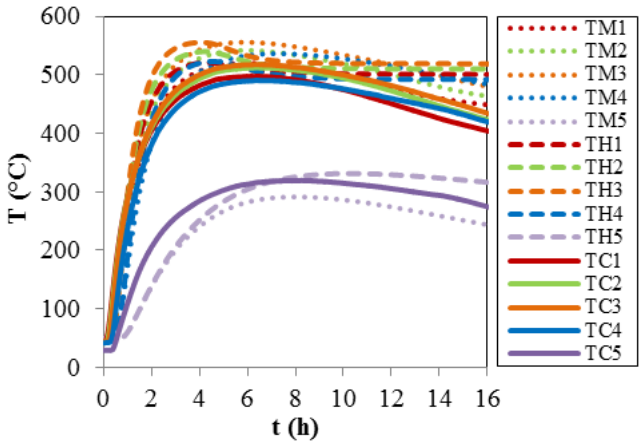

Fig. 12 Temperature readings for thermocouples (TC) and the temperature predictions from simulations with thermomechanical (TM) and thermohydraulic models (TH)

Carbon segregation ratio profiles along the ingot centerline were quantitatively compared between simulation results and experimental measurements, as given in Figure 13a. The y-axis was set as the distance from the hot-top/ingot interface section. It can be noted that the thermomechanic chemical predictions matched better the experimental results in the hot-top as well as in the upper part of the ingot. The strong carbon positive segregation at the top center of the hot-top and the lower segregation intensity in the ingot were well reproduced. For the TH model, at the top center of the hot-top, the carbon concentrations were overestimated and in the upper part of the ingot, the segregation severity varied dramatically from the test results.

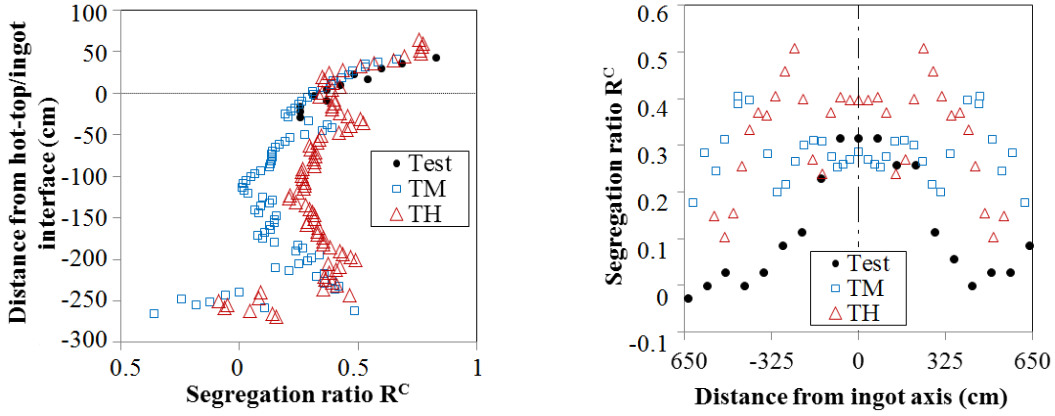

(a) (b)

Fig. 13 Evolution of macrosegregation ratio of carbon at the end of solidification. **a** Along the ingot centerline. **b** **A**long the cutting section with 30cm below the hot-top/ingot body interface

Chemical variation examination along the transverse cutting section, 30cm below the hot-top/ingot separation interface, confirmed the better predictability of the TM model, as shown in Figure 13b. The positive solute bands between the center and the ingot wall were predicted by both models. But the same regions were not detected by experimental measurements. This difference could be related to the fact that measured sampling points were not sufficient for inspection of finer segregation structures.

Macrosegregation ratio patterns of carbon predicted by both models were compared with mass spectrometer measurements and the results are presented in Figure 14. As shown in Figures 14a and 14b, the solute-enriched zone between the center and the ingot wall predicted by TM model matched better the area enclosed by the two black solute-enriched bands in Figure 14c. However, it was not possible to capture enough details about the size and the number of positively segregated channels with any of the two models. Indeed, in order to attain a high spatial resolution in a relatively small scale (a few centimeters), a very high grid resolution is required, which was not the case in the present study.

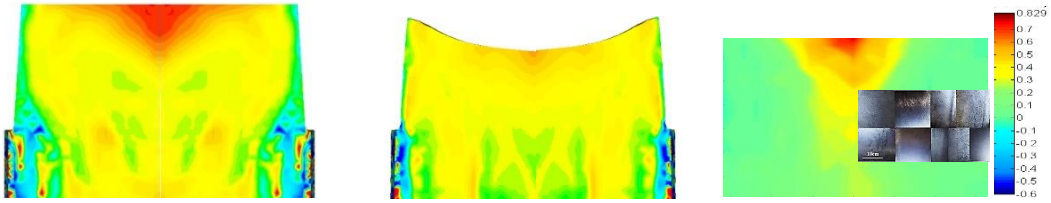

(a) (b) (c)

Fig. 14 Segregation ratio patterns of carbon on the axial surface of longitudinal section. **a** thermohydraulic model (TH). **b** Thermomechanic model (TM). **c** Mass spectrometer measurements with macrostructure around the hot-top/ingot junction

It can be seen that the TM model predictions agree better with experimental results than the TH model. Based on the above discussions, this is probably due to the fact that the TM model considered solid deformation features during solidification, which is ignored by the TH model. These features include the formation of the shrinkage cavity at the top and the air gap between casting shell and mold. They result in the reduction of global volume and the change of heat transfer mode from purely conduction to convection and radiation. These changes correspond to characteristics closer to the actual solidification phenomena, in the temperature gradient, liquid fraction distribution, fluid flow field, solidification time, and macrosegregation pattern, compared to those predicted with the TH model. As a result, a better agreement with experimental measurements was obtained by the TM model.

6 Conclusion

In the present work, the effect of liquid contraction, solid shrinkage and air gap formation on macrosegregation patterns during casting and solidification of large size steel ingots was investigated. A thermohydraulic model (TH), based on natural convection, and a thermomechanic model (TM), considering both convection and solidification shrinkage, were developed and the obtained simulation results were validated with experimental measurements. The following conclusions can be drawn from the present study:
- Temperature gradients, liquid flow pattern and macrosegregation patterns in the casting are primarily dominated by buoyancy effects (i.e. natural convection).
- The formation of the shrinkage cavity at the top and the air gap between casting shell and mold modified the inclination of isotherms and solidification front, the iso-f_l area, the initiation of solidification and the total time for solidification.
- The divergence and the disorder in the fluid flow generated by volume change influences the solutal redistribution in the melt and impacts the final macrosegregation patterns.
- The model accounting for the combined influence of buoyancy and shrinkage (the TM model) presents a better quantitative and qualitative match with the thermal, chemical and dimensional experimental results, when compared with the case neglecting shrinkage effect and air gap formation (the TH model).

This study permits to better understand the impact of thermomechanical shrinkage in ingot cooling process and could be used in industry to improve the quality of large size ingot production and the productivity of high value added steels or other alloys.

As a preliminary result for the coupling prediction of segregation and shrinkage, more effort is still needed, like the determination of actual mold material properties, the improvement of grid resolution and additional development to describe grain nucleation, growth and the morphology transition between globular and dendritic grains during solidification. To realize the possible prediction of mesosegregation and grain structure formation and transition, particularly in large size ingots, there is still a long way to go.

Acknowledgements The financial support from the Natural Sciences and Engineering Research Council (NSERC) of Canada in the form of a Collaborative Research and Development Grant (CRDG) under number 470174 is gratefully acknowledged. Finkl Steel-Sorel Co. for providing the material is greatly appreciated.

References

1. ASM Handbook Volume 11: Failure Analysis and Prevention (2002) ed. by Becker WT, Shipley RJ, ASM International, Materials Park, OH, USA, pp. 5-81
2. Loucif A, Ben Fredj E, Harris N, Shahriari D, Jahazi M, Lapierre-Boire LP (2018) Evolution of A-type macrosegregation in large size steel ingot after multistep forging and heat treatment. Metall Mater Trans B 49:1046-1055
3. Fleming MC, Nereo GE (1967) Macrosegregation: Part I. Trans. Metall Soc AIME 239:1449-1461
4. Im IT, Kim WS, Lee KS (2001) A unified analysis of filling and solidification in casting with natural convection. Int J Heat Mass Tran 44:1507-1515
5. Sang BG, Kang XH, Liu DR, Li DZ (2010) Study on macrosegregation in heavy steel ingots. Int J Cast Met Res 23(4):205-210
6. Li J, Wu M, Ludwig A, Kharicha A (2012) Modelling macrosegregation in a 2.45 ton steel ingot. IOP Conf Ser: Mater Sci Eng 33:012091
7. Combeau H, Kumar A, Založnik M, Poitrault I, Lacagne G, Gingell A, Mazet T, Lesoult G (2012) Macrosegregation prediction in a 65 ton steel ingot. 1st International Conference on Ingot Casting, Rolling and Forging, Aachen, Germany, Brüssel-Saal, Ingot Casting - Simultion, June
8. Combeau H, Založnik M, Hans S, Richy PE (2009) Prediction of macrosegregation in steel ingots: Influence of the motion and the morphology of equiaxed grains. Metall Mater Trans B 40:289-304
9. Wu M, Ludwig A (2009) Modeling equiaxed solidification with melt convection and grain sedimentation-I: Model description. Acta Mater 57:5621-5631
10. Beckermann C (2002) Modelling of macrosegregation: applications and future needs. Int Mater Rev 47 (5):243-261
11. Chiang FC, Tsai HL (1992) Transport phenomena in Material Processing, ASME HTD vol.132, ed. by M. Charmichi, M.k. Chyu, Y. Joshi, S.M. Walsh, ASME, Fairfield, NJ, pp.153-222
12. Gao Z, Jie W, Liu Y, Luo H (2017) Solidification modelling for coupling prediction of porosity and segregation. Acta Mater.127 : 277-286
13. Heinrich JC, Poirier DR (2004) The effect of volume change during directional solidification of binary alloys. Modell Simul Mater Sci Eng 12(5):881-899
14. Ehlen G, Ludwig A, Sahm PR, Buhrig-Polaczek A (2003) Split-solid-model to simulate the formation of shrinkage cavities and macrosegregations in steel casting. Modelling of Casting, Welding and Advanced Solidification Processes X. ed. by Stefanescu DM, Warren J, Jolly M, Krane M. TMS The Minerals, Metals & Materials Society 285-292
15. Lan P, Zhang JQ (2014) Numerical analysis of macrosegregation and shrinkage porosity in large steel ingot. Ironmak. & Steelmak. 41(8):598-606
16. Reikher A, Gerber H, Pillai KM, Jen TC (2010) Natural convection - An overlooked phenomenon of the solidification process. Die Cast Eng 1:28-31
17. Duan Z, Tu W, Shen B, Shen H, Liu B (2016) Experimental measurements for numerical simulation of macrosegregation in a 36-ton steel ingot. Metall Mater Trans A 47:3597-3605
18. MATLAB and Statistics Toolbox Release 2012b, The MathWorks Inc., Natick, Massachusetts, United States, 2012
19. TherCast 8.2®,Transvalor, S.A., Cedex, France

20. Schneider MC, Beckermann C (1995) Formation of macrosegregation by multicomponent thermosolutal convection during solidification of steel. Metall Mater Trans A 26:2373-2388
21. Wu M, Ludwig A, Fjeld A (2010) Modelling mixed columnar-equiaxed solidification with melt convection and grain sedimentation - Part II: Illustrative modelling results and parameter studies. Comput Mater Sci 50:43-58
22. Andersson JO, Helander T, Höglund L, Shi PF, Sundman B (2002) Thermo-Calc & DICTRA, computational tools for materials science. Calphad 26:273-321
23. Miettinen J (1997) Calculation of solidification-related thermpphysical properties for steels. Metall Mater Trans B 28:281-297
24. Mills KC (2002) Recommended values of thermophysicalpProperties for selected commercial alloys. Woodhead Publishing Ltd. pp.112
25. Physical constants of some commercial steels at Elevated Temperatures, BISRA/Butterworths Scientific
26. Thermal properties of metals, conductivity, thermal expansion, specific heat. Metal products distributor supplier. Http://www.engineersedge.com/properties of metals.htm
27. Dong Q, Zhang J, Yin Y, Wang B (2017) Three-dimensional numerical modeling of macrosegregation in continuously cast billets. Met 7:1-22. doi:10.3390/met7060209
28. Qian S, Hu X, Cao Y, Kang X, Li D (2015) Hot top design and its influence on feeder channel segregates in 100-ton steel ingots. Mater Des 87:205-214
29. Schneider MC, Beckermann C (1995) A numerical study of the combined effects of microsegregation, mushy zone permeability and flow, caused by volume contraction and thermosolutal convection, on macrosegregation and eutectic formation in binary alloy solidification. Int J Heat Mass Transfer 38:3455-3473

Appendix 1 Nomenclature

Parameters	Symbols	Parameters	Symbols
Segregation ratio of solute *i*	R^i	Reference temperature (liquidus) (°C)	T_{ref}
Local concentration of solute *i*	ω^i	Solutal expansion coefficient of solute *i* ($\times 10^{-2}$/wt.%)	β_{ω^i}
Nominal concentration of solute *i* (wt.%)	ω_0^i	Liquid fraction	f_l
Temperature (°C)	T	Solid fraction	f_s
Melting temperature of pure iron (°C)	T_m	Solid density (kg/m^3)	ρ_s
Liquidus slope of solute *i* (K/wt.%)	m_l^i	Density (kg/m^3)	ρ
Concentration of solute *i* in the liquid	ω_l^i	Specific heat capacity (J/Kg/(°C)	C_P
Number of solute elements	N	Volume fraction of δ-ferrite	f_δ
Heat flux	q	Volume fraction of γ-austenite	f_γ
Thermal conductivity (W/m/K)	λ	Yield stress (MPa)	σ_s
Heat transfer coefficient (W/m/°C)	h	Young's modulus (GPa)	E
Emissivity	ε_T	Strain hardening exponent	n
Stephan-Boltzmann constant ((=5.776×10^{-8}W/m^2/K)	σ_T	Strain-rate sensitivity coefficient	m
Exterior environmental temperature (°C)	T_{ext}	Solute partition coefficient of solute element *i*	k^i
Solute flux	j	Latent heat of fusion(KJ/Kg)	L_f
Diffusion coefficient of solute *i* in the liquid (mm^2/s)	D_l^i	Enthalpy of reaction (KJ/kg)	ΔH
Density of liquid (kg/m^3)	ρ_l	Steel pouring temperature (°C)	T_0
Reference density (kg/m^3)	ρ_0	Initial temperature of molds, powders and refractory (°C)	T_{mold}

Thermal expansion coefficient (/K)	β_T	Filling time (min)	t